applied sciences

IMPACT FACTOR 2.9

CITESCORE 6.1

Article

Detecting Karstic Cavities Utilizing Electrical Resistivity Imaging (ERI) in Antalya, Türkiye

Fatih Uçar and Özgür Aktürk

MDPI

https://doi.org/10.3390/app16146948

applied sciences

MDPI

Article

Detecting Karstic Cavities Utilizing Electrical Resistivity Imaging (ERI) in Antalya, Türkiye

Fatih Uçar * and Özgür Aktürk

Department of Geological Engineering, Faculty of Engineering, Akdeniz University, Dumlupınar Blvd., Campus, Antalya 07058, Türkiye; akturko@akdeniz.edu.tr
* Correspondence: fatihucar@akdeniz.edu.tr

Abstract

Residual soil often collapses over bedrock cavities during construction in karst areas. This happens especially when excavation reduces the thickness of the unconsolidated cover beds layer. This phenomenon is exacerbated by the inherent complexities of karst environments. The uncertainty surrounding the depth, size, and geometry of subterranean voids renders detailed geotechnical analysis problematic, thereby complicating risk assessment and mitigation strategies for construction projects in these areas. To overcome the problem of detecting subsurface cavities, this study utilized two-dimensional Electrical Resistivity Imaging (ERI) on Antalya tufa units. Vertical Electrical Sounding (VES), a traditional one-dimensional method for resistivity studies, was also used as a supplementary method in this research. Karst units with cavities are formed by melting primary units with atmospheric waters. These cavities may be filled with clay, water, or air, affecting resistivity values. Studying air-filled cavities is the main purpose of this work. Experimental results were compared with the visual appearance of air-filled cavities; they indicated that air-filled cavities correspond to high resistivity values (~15,000 ohm.m). The ERI method can detect subsurface cavities in terms of its accuracy, resolution, required field effort, and ease of data analysis.

Keywords: Antalya tufa; Electrical Resistivity Imaging (ERI); karstic cavity; subsurface investigation; Vertical Electrical Sounding (VES)

1. Introduction

The stability of residual soil overlying solution cavities in carbonate rocks is often a concern in karst areas. This issue is important during site selection, construction, and facility maintenance. These processes are of great concern for the stability of unconsolidated cover beds above the cavities formed by the dissolution of carbonate rocks. Investigating cavities on the karst terrain is a significant study in geotechnical/geophysical/civil engineering and hydrogeology. Settlement or collapse problems because of karst cavities can significantly impact infrastructure and construction [1]. Karst characteristics (fractures and cavities) constitute a high risk in construction engineering because they directly affect the geomechanical properties of the soil/rock [2]. The progressive dissolution of soluble rock at deep zones through groundwater infiltration may result in subsidence of the overburden and the development of soil cavities or domes close to rock contact zones [3]. The general subsurface profile of karst terrain comprises five layers defined in Sowers [3] (Figure 1). The first layer (closest to the surface) is a remolded, unstructured part whose hardness varies significantly because of being in near-surface conditions. Layers 2 and 3 are defined

Check for updates

Academic Editor: Nikolaos Koukouzas

Received: 28 May 2026
Revised: 4 July 2026
Accepted: 6 July 2026
Published: 10 July 2026

Copyright: © 2026 by the authors. Licensee MDPI, Basel, Switzerland. This article is an open access article distributed under the terms and conditions of the Creative Commons Attribution (CC BY) license.

as residual soil, with their overconsolidation ratio and strength. Layer 2 is more significant than Layer 3 in those characteristics. As is seen, the strength of the soil decreases with deeper points, which is a common characteristic of karst terrain. This is called an "inverted strength profile" because residual soils generally become stronger with increasing depth, in contrast to the karst terrain. The thickness of Layer 2 may differ between 1 and 50 m, and Layer 3's may be between 1.5 and 5 m. Randomly distributed rock pinnacles containing rock blocks and soft soils are generally the contents of Layer 4 and may contain voids or soil domes, as in Figure 1. The competent carbonate rock of this formation is Layer 5, which exhibits too high strength relative to the soil parts but may contain expanded joints, fractures, or caves with a solution process; because of these joints, it is often hydraulically active.

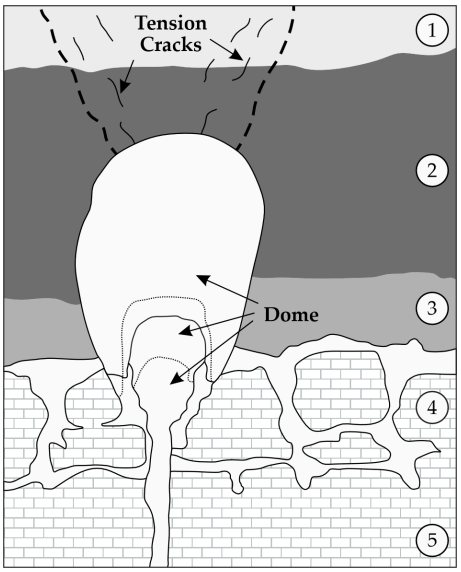

Figure 1. Idealized subsurface profile in karst, with enlarging soil void or dome above bedrock [3,4]: Layer 1, remolded structureless layer with highly variable stiffness; Layer 2, overconsolidated residual soil; Layer 3, normally or lightly overconsolidated residual soil; Layer 4, randomly distributed rock pinnacles, rock blocks with soft soils, and voids or soil domes; and Layer 5, hydraulically active competent limestone. (Not to scale).

As illustrated in Figure 1, dissolution-induced cavities within soluble carbonate bedrock (Layer 5) progressively enlarge (Layer 4) and create zones of reduced geotechnical stability. The upward propagation of these voids, often manifested as dome-shaped cavity roofs, is primarily associated with the dissolution of carbonate rocks such as limestone. As cavity enlargement continues, instability is transferred to the overlying overconsolidated residual soils (Layers 2 and 3), increasing the potential for subsidence and collapse. Furthermore, the progressive development of subsurface cavities may induce tensile stresses within the overburden, resulting in the formation of tension cracks that can extend to the surficial cover deposits (Layer 1).

The Antalya Basin developed unconformably over a subsided basement and is bounded by Mesozoic autochthonous carbonate platforms, represented by the Beydağları platform to the west and the Anamas–Akseki platform to the east [5]. Paleogeographic reconstructions indicate that the western sector was characterized by an eastward transition from the extensive Beydağları carbonate platform into an oceanic basin containing isolated carbonate structures. The northern sector preserves remnants of several carbonate platform successions, whereas the eastern and southeastern sectors exhibit evidence of a westward transition from another major carbonate platform margin toward the basin interior, reflecting the complex paleogeographic evolution of the region during the Mesozoic [6]. The Antalya tufa deposits originated through coupled physicochemical and biogenic car-

bonate precipitation processes. Their highly porous fabric consists of carbonate grains bound by thin meniscus cements formed by calcium carbonate precipitates. These cement bridges are particularly vulnerable to dissolution by infiltrating meteoric waters and other low-mineralized water sources. The progressive removal of carbonate cement reduces interparticle cohesion and destabilizes the tufa framework, promoting an increase in secondary porosity and the coalescence of pre-existing voids. As a result, the geomechanical properties of the deposit deteriorate, significantly increasing its susceptibility to subsidence and collapse [7]. Karst formations arise from the dissolution of soluble rocks such as limestone, salt, gypsum, etc., and tension cracks and subsurface drainages represent them. Groundwater in subsurface cavities (saturated zone) drains to the surface, which has an example at Kırkgöz Springs, Antalya (Figure 2). Almost all karst formations result from collapse triggered by subsurface cavities formed by the dissolution of soluble rocks [8]. The solubility of limestones has become more attractive in engineering because of their wide distribution on the surface compared to other soluble rocks [3]. Tufa/Travertine is defined as secondary $CaCO_3$ deposits containing plant, animal remains, and bacteria precipitated by biological or physicochemical processes [9]. Tufa/Travertine units were deposited by wrapping the plants between the glacial periods of the Pleistocene and had a porous appearance because of the decay activities in those plants. It is also known that Tufa/Travertine units develop solution cavities [10]. Because the solution cavities in karst systems are hydrologically connected, these variations in the groundwater (seasonal or unusual) will result in the residual soil above the rock cavity softening and eroding, with the soil dome gradually forming and enlarging (Figure 1). The transfer of pressure from a collapsing mass of cover beds onto steady neighbor soil parts is called the arching effect [11]. This occurs in shallow overburden where arching cannot occur; tensile stresses arise in the residual soil, which can cause surface cracks and collapse of the dome. A significant correlation between periods of above-average precipitation and increased frequency of sinkhole formations in highway ditch lines was established by Moore [12]. Furthermore, an elevated incidence of sinkholes during drought periods was observed and attributed to the lowering of the water table. Moore [13] subsequently demonstrated that the developmental patterns of underlying solution cavities and resultant caves generally reflect the bedrock's attitude, fracture density, and groundwater movement, as these patterns mirror the fracture network within the bedrock.

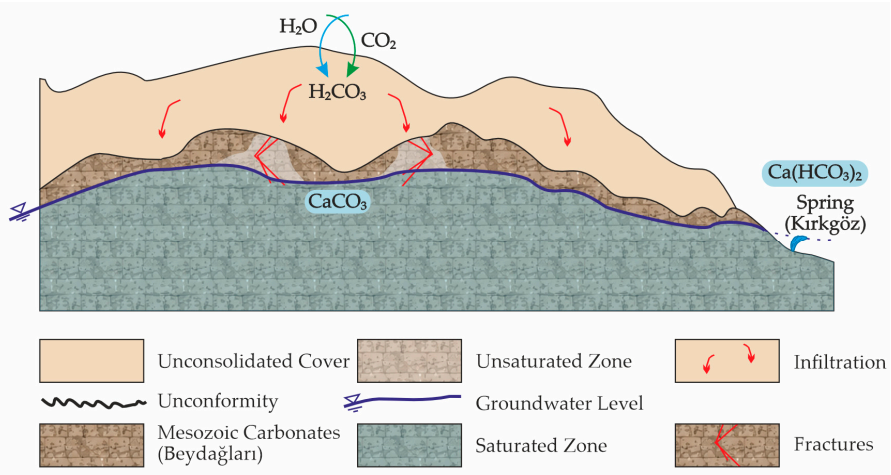

Figure 2. Conceptual model illustrating the karstification process, including progressive limestone dissolution and groundwater spring emergence. (Not to scale).

In karst terrains, anthropogenic alterations to groundwater levels have been extensively documented as catalysts for sinkhole formation [14–18]. These alterations predom-

inantly stem from three main sources: (1) increased urbanization, leading to changes in surface water drainage and groundwater recharge patterns; (2) agricultural practices, particularly irrigation and land-use changes, which can modify local hydrological regimes; and (3) mining activities, which may directly impact subsurface hydrology through dewatering processes or indirectly through alterations to surface topography and drainage networks. In the absence of anthropogenic disturbances, particularly construction activities that alter surface hydrology or reduce the thickness of the overburden, the residual soils overlying solution cavities may maintain stability and exhibit significant load-bearing capacity. These soils can potentially support substantial additional surface loading without compromising structural integrity. However, site development often necessitates excavation and grading, which can significantly reduce the thickness of the overburden. This reduction in soil cover thickness may potentially destabilize the underlying karst features, increasing the risk of sinkhole formation or subsidence.

In the development of specific infrastructure facilities in karst terrains, such as waste management installations, ash/refuse landfills, or water reservoirs, the economic viability is intrinsically linked to their storage capacity. This economic imperative often necessitates the removal of substantial volumes of overburden soil, potentially exacerbating the risks associated with karst geology. The maximal excavation of overburden to increase storage capacity must be carefully balanced against the need to maintain adequate soil cover for stability and environmental protection. This balance requires comprehensive geotechnical investigations, advanced modeling techniques, and the implementation of robust engineering solutions to mitigate the heightened risks of sinkhole formation or subsidence in these critical facilities. This directly conflicts with subsurface stability considerations, thus making overburden thickness an issue during site selection and preliminary design [4,19].

Further investigations [3,20] have revealed a striking disparity between the size of initiating rock cavities and the resultant surface expressions. These studies indicate that sinkholes can manifest above relatively small rock openings, with rock cavities as minimal as 150 mm in diameter, potentially giving rise to soil domes exceeding 15 m in diameter. However, this phenomenon is contingent upon two critical factors: (1) the surrounding soil matrix must exhibit exceptionally low strength characteristics, and (2) there must be substantial groundwater movement within the underlying rock caverns. These findings underscore the critical importance of comprehensive subsurface characterization and hydrological assessment in karst terrains, particularly in areas slated for development or infrastructure projects.

The research on Tufa/Travertine in Turkey, particularly in Antalya, holds significant importance [7,9,10,21–25]. Antalya, a prominent tourism city in Turkey, necessitates the construction of high-rise buildings and hotels. The hidden porous structure of the Antalya Tufa, which is not visible from the surface in most areas, poses a potential threat to these constructions. The stability of the Antalya sea cliff, another crucial city area, also requires investigation due to its porous structure [10].

The early detection of the depth/size/geometry of subterranean voids is of utmost importance, particularly in densely populated cities like Antalya. Expanding these voids can lead to hazardous situations during or after construction and infrastructure work. While some cavities are accessible from the daylight surface, allowing for direct mapping of their structures, many others are deeply buried and disconnected. In such cases, geophysical methods are imperative to indirectly describe these caves [1]. Recent studies have further highlighted the importance of accurately characterizing subsurface cavities and discontinuities because they significantly influence the mechanical behavior and stability of rock masses under engineering loading conditions [26]. Although these studies primarily focus on rock mechanics, they emphasize the necessity of reliable subsurface detection methods

prior to engineering design. Geophysical methods have been widely applied for the detection and characterization of sinkholes and concealed karst features, providing valuable information for engineering site investigations and hazard assessment in karst terrains. Among these methods, Electrical Resistivity Imaging (ERI) has become one of the most widely used techniques because of its ability to delineate subsurface resistivity variations associated with karst cavities [27]. Recent studies have further demonstrated that fluid–rock interactions and karstification processes can significantly degrade the physico-mechanical properties of carbonate rocks, thereby increasing the susceptibility to sinkhole development and geotechnical instability. These findings further emphasize the importance of reliable geophysical methods for the early detection and characterization of concealed karst cavities prior to engineering design and construction [28]. The present study is intentionally focused on shallow tufa karst and near-surface dissolution cavities of direct engineering relevance. Rather than targeting deep regional karst systems, the objective is to evaluate the effectiveness of ERI and VES for engineering-scale investigations where accurate delineation of shallow cavities is essential for site characterization and foundation planning. Because the investigated sinkhole hazards are generated within the shallow weathered tufa horizon, a survey depth of approximately 3–4 m was considered sufficient to image the target dissolution cavities. The application of geophysical methods to karst investigations has increasingly shifted from simple cavity detection toward integrated engineering site characterization. Recent studies have shown that ERI is capable of accurately delineating shallow karst cavities and dissolution features, particularly when supported by complementary geophysical techniques. Such integrated approaches improve the identification of subsurface geohazards and provide valuable information for engineering planning and risk assessment in karst terrains [29]. Karst terrains pose significant challenges for engineering projects because concealed dissolution cavities and sinkhole development may compromise the stability of buildings, transportation infrastructure, and other engineering structures. Consequently, reliable characterization of near-surface karst systems has become an essential component of engineering site investigations. Recent studies have demonstrated that Electrical Resistivity Imaging (ERI) provides an effective, non-invasive approach for detecting concealed karst cavities, delineating dissolution zones, and supporting hazard assessment in carbonate terrains, particularly when integrated with geological observations and borehole information [30]. The increasing application of high-resolution geophysical methods demonstrates that concealed cavities can be effectively investigated without destructive excavation. Recent studies have shown that Electrical Resistivity Imaging (ERI), either alone or integrated with complementary geophysical techniques, provides reliable information on cavity location, geometry, and surrounding geological conditions, thereby supporting both scientific investigations and engineering decision-making [31]. Despite these recent advances, relatively few studies have focused on the detection and characterization of shallow air-filled cavities developed within tufa deposits under engineering-scale site conditions using integrated ERI and VES investigations.

The city of Antalya is in the southwestern part of Turkey and is situated on the Mediterranean coast. The city center is mainly founded on rocks specified as tufa rather than traditional travertine [32]. The process of tufa/travertine starts with the reaction of carbon dioxide (CO_2) and rainwater (H_2O). As a result, carbonic acid (H_2CO_3) is formed (Figure 2) (Equation (1)). Then, carbonic acid (H_2CO_3) interacts with the limestone unit ($CaCO_3$), so the calcium bicarbonate ($Ca(HCO_3)_2$) is formed (Figure 2) (Equation (2)). The tufa/travertine unit is formed by the reprecipitation of calcium bicarbonate ($Ca(HCO_3)_2$) (Equation (3)). Therefore, tufa/travertine is the secondary product of calcareous rocks. Both tufa and travertine are formed from calcium carbonate ($CaCO_3$) rocks deposited in freshwater environments [32]. These calcium carbonate rocks are categorized into two

main groups—hot-water and cool-water deposits—wherein travertine represents thermal deposits (>20 °C) [21] and tufa represents ambient temperature deposits [32].

$$H_2O + CO_2 \rightarrow H_2CO_3(\text{CarbonicAcid}) \quad (1)$$

$$H_2CO_3 + CaCO_3(\text{Limestone}) \rightarrow Ca(HCO_3)_2(\text{CalciumBicarbonate}) \quad (2)$$

$$Ca(HCO_3)_2 \rightarrow CaCO_3(\text{Tufa/Travertine}) + H_2O + CO_2 \quad (3)$$

The area's hydrological regime, topography, and regional and local geology are controlled by the structure settled in the Late Pliocene. Tufas are exposed in this region, especially on cliffs, slopes, narrow valleys, and road cuts [21]. The primary tufa caves formed during the tufa process, and the secondary karst cavities formed by melting with atmospheric waters are mostly filled with soil formations representing the cessation period of the tufa cycle. These soil zones were mainly developed on well-consolidated tufas [9].

Geophysical methods are widely used for engineering surveys like subsurface cavities (air/water/clay-filled), buried structures, faults, and fissures [33]. Although several geophysical investigation methods can identify subsurface geological structures, Electrical Resistivity Imaging (ERI) is one of the most popular methods for detecting shallow subsurface anomalies [34–36]. ERI is an efficient technique for determining the boundaries of cavities with soil/rocks because cavities show completely different electrical resistivity values from other subterranean neighboring units [2,37–39]. ERI indicates different resistivity values depending on the saturation conditions of the analyzed caves. It is essential to determine whether the cave is filled or not with any material. Air-filled cavities show high resistivity values, while water-filled cavities show lower values [37]. Moreover, fresh groundwater (10–100 ohm.m) and seawater (0.1–1 ohm.m) also indicate different resistivity values [40]. ERI is a continuous image of the subsurface of geological structures and produces better results than traditional methods. Moreover, all geophysical methods, notably ERI, can be applied as non-invasive methods in fields or protected areas where mechanical drilling is impossible [10]. Among the available near-surface geophysical methods, Electrical Resistivity Imaging (ERI) has gained widespread acceptance for karst investigations because it provides an effective compromise between investigation depth and spatial resolution while being highly sensitive to subsurface resistivity variations associated with cavities, fractures, and groundwater conditions. These characteristics make ERI particularly suitable for engineering-scale investigations of shallow karst systems [30]. Additionally, the accuracy of depth analysis can be ensured by using Vertical Electrical Sounding (VES) [41–45]. Both geophysical methods make it possible to determine the boundaries between geological structures and detect karst cavities. The main objective of this research is to identify subsurface karst characteristics (e.g., cavities) by utilizing the two-dimensional ERI method, and VES is used as a supplementary method. Since the topographic cross-section of air-filled cavities can be clearly seen in the study area, this provided an excellent opportunity to validate ERI and VES results with the visual appearance of karstic cavities.

2. Study Area and Geological Setting

2.1. Study Area

The city of Antalya is on the coast of the Mediterranean Sea. The ERI measurements were taken at Antalya, Kepez County, Turkey, which was chosen as the study area (Figure 3a, white dotted circle) because it has a mountainous appearance and contains structures with visible cavities (Figure 3), and was selected for the measurements since the topographic cross-section of air-filled cavities can be clearly seen (Figure 3b,c). The measurements were

taken at two different locations where Kepez-1 was located at 36.934156° N, 30.687046° E, and Kepez-2 was located at 36.937716° N, 30.688924° E (Figure 3b,c), and the presence of air-filled cavities was determined by considering resistivity values.

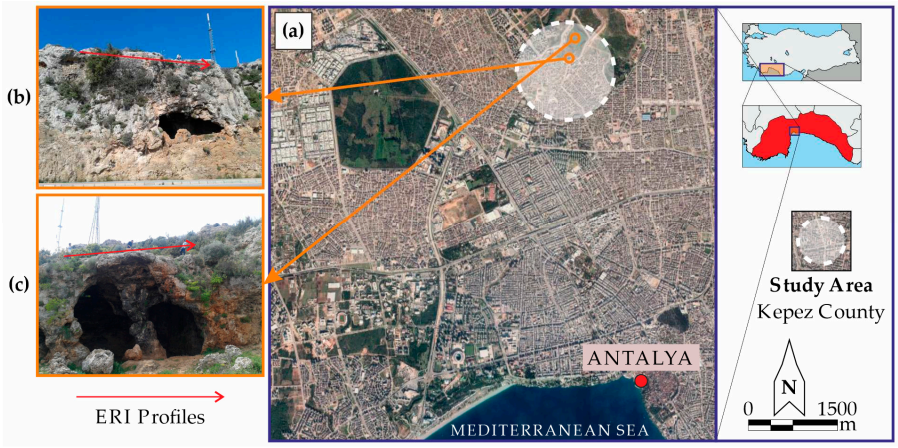

Figure 3. (**a**) Location of study areas at Kepez County and ERI profiles: (**b**) Kepez-1 profile; (**c**) Kepez-2 profile.

2.2. Geological Setting

Beydağları border the Antalya Tufas at the west-northwest boundary, the Aksu River at the east boundary, and the Mediterranean Sea to the south topographically (Figure 4). The basin looks like a depression area at the base of the Beydağları. The city center is mainly founded on calcareous rocks.

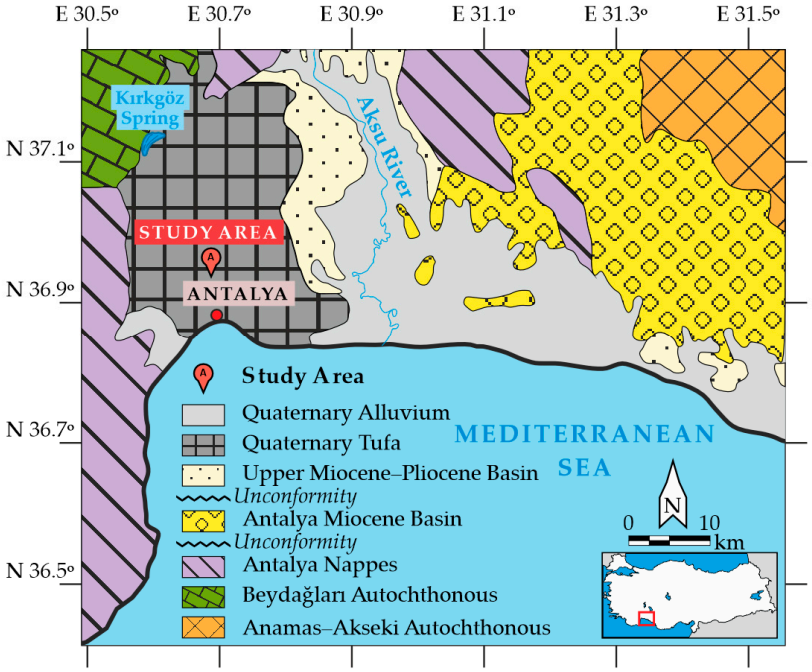

Figure 4. Geological map of the city of Antalya and its surrounding area [23,46].

The primary rock units in Antalya and its surroundings are described in two ways: autochthonous and allochthonous [46] (Figure 4). The autochthonous are Anamas–Akseki (deposited between Cambrian to Eocene age), situated in the eastern part, and Beydağları (deposited between Jurassic to Miocene age), situated in the northwestern part of the city (Figure 4). Both units comprise platform-type carbonate sediments [23]. The allochthonous groups are the Antalya Miocene basin (sandstone, conglomerate, limestone, claystone,

and shale) and Upper Miocene–Pliocene basin (conglomerate, sandstone, and limestone) (Figure 4) [46,47]. The Antalya Nappes, as the primary allochthonous of the region, play a crucial role in understanding the geological history.

Calcareous rocks—the dominant lithology and outcropping widely in the residential area—are referred to as Antalya Tufa [32]. Calcium Bicarbonate, which was transmitted from the limestone in the Beydağları and flowed from Kırkgöz springs, reprecipitated in an area of 600 km^2 and formed the Antalya Tufa, known as the world's largest known tufa deposit [48]. Sediments deposited from cool spring waters are secondary products of calcareous rocks and reach a total thickness of up to 250 m [21]. Pentecost and Lord [49] approve of a botanical approach for tufa classification, while Ordóñez and García del Cura [50] and Chafetz and Folk [51] agree with the geomorphological and petrographical approaches [22]. Pedley [52] defines Antalya tufas according to geomorphological and petrographical approaches because they seem more appropriate.

3. Materials and Methods

Multiple geophysical methods to collect extensive geophysical data from the study area may be used. These methods serve two main purposes. First, an initial field investigation of the entire area can be conducted with electromagnetic-conductivity, magnetometry, and gamma-ray spectrometry methods to map the site and identify near-surface geological features. Second, electrical-resistivity methods (ERI or VES) [53] and microgravity surveys may be performed along a selected profile across the research area. These surveys aimed to gather information about unknown cavities or unreachable parts of known caves [54].

3.1. Electrical Resistivity

Resistivity is one of the distinguishing characteristics of geological materials. Most rock-forming minerals and compact rocks are bad conductors. Because the electric current is carried through a material by the transmission of ions in pore waters, the porosity and degree of saturation differ in the resistivity of materials. Increasing electrical resistivity as the porosity of the material decreases is an example of this situation. The deviations of potential differences determine the anomalies of subsurface materials [55].

Essentially, all electrical resistivity methods are based on Ohm's Law, which declares that the current in an electrical circuit is directly proportional to the potential and inversely proportional to the resistance of the material (Equation (4)). Additionally, according to Ohm's Law, the resistance of the material is associated with its length, area, and resistivity (Equation (5)):

$$V = I \cdot R \tag{4}$$

$$R = \rho \cdot (r/A) \tag{5}$$

where R represents resistance, V is potential, I is current, r is length, A is area, and ϱ is the resistivity of the material. Equations (4) and (5) are rearranged in terms of the resistance value. The combined formula is shown in Equation (6):

$$V/I = \rho \cdot (r/A) \tag{6}$$

It is assumed in resistivity studies that current lines travel along a half-sphere and penetrate the subsurface. Consequently, the A value is equal to the half-sphere's area ($2\pi r^2$), and the potential is rewritten in terms of other parameters (Equation (7)):

$$V = (I \cdot \rho)/(2 \cdot \pi \cdot r) \tag{7}$$

3.2. Vertical Electrical Sounding (VES)

One-dimensional (1D) resistivity survey or electrical drilling is a resistivity method that applies current and potential electrodes along a straight line at the defined spacing around a fixed central point [55]. It is also known as Vertical Electrical Sounding (VES), as it analyzes vertical values in 1D resistivity surveys [33].

The primary purpose of the method is to penetrate the current deeper by increasing the distance between the current electrodes. It is used to detect the resistivity values of horizontal layers on a vertical profile and helps identify loose horizontal overburden thickness over rocks [55].

3.3. Electrical Resistivity Imaging (ERI)

ERI is a specific resistivity method for subsurface investigations [38]. The system injects electrical current into the ground with an electrode couple (current electrodes, A-B). It measures the potential difference in the ground with another electrode couple (potential electrodes, M-N) (Figure 5). This is handled by laying out the electrodes along a straight profile, using a specific electrode interval. The distance between electrodes is determined by a selected electrode array, as shown in Figure 5a for Wenner Alpha and Figure 5b for Wenner–Schlumberger. While the distance between the current and the potential electrodes is fixed in the Wenner Alpha analysis (Figure 5c), this distance differs in the Wenner–Schlumberger analysis (Figure 5d) for different data levels. Electrode interval is an important issue in ERI analysis because it affects the analysis's resolution, the depth of the pseudosection image, and the accuracy of measurement and computation. If high resolution is required, the electrode interval is narrowed; however, this process reduces the depth of the visual image. In contrast, wider electrode intervals make the resulting image deeper and have a lower resolution. Every measurement in the set of measurements is defined as a station. Figure 5e shows the possible sequence of measurements for the Wenner Alpha electrode array for a system with 20 electrodes. All data levels in resistivity measurements end at the last electrode in the line used.

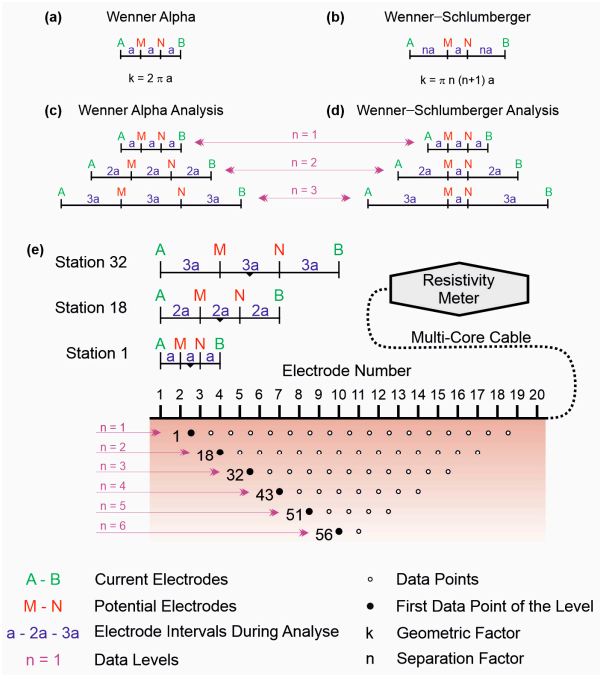

Figure 5. (**a**) Specific array geometry for Wenner Alpha; (**b**) Specific array geometry for Wenner–Schlumberger; (**c**) Specific array geometry during Wenner Alpha analysis; (**d**) Specific array geometry during Wenner–Schlumberger analysis; and (**e**) Arrangement of electrodes for a 2D electrical survey and the sequence of measurements used to build up a pseudosection [40].

The Wenner Alpha and Wenner–Schlumberger configurations were selected because providing high signal-to-noise ratio and good sensitivity to subhorizontal resistivity variations, making them suitable for detecting shallow dissolution cavities in relatively homogeneous tufa deposits.

Forward modeling is used to calculate apparent resistivity pseudosection data for the testing site. For complex geological structures, apparent resistivity values can be calculated using numerical methods [56]. These methods include finite differences [57–59], finite elements [60], and integral equations [61]. The acquired resistance measurements are subsequently transformed into apparent resistivity values through multiplication with array-specific geometric factors, which are determined by the electrode configuration employed in the survey. These apparent resistivity values undergo an inversion process to derive the true subsurface resistivity distribution, enabling the delineation of individual resistivity layers' thickness and depth within the subsurface profile. Inversion represents a fundamental component of contemporary resistivity imaging methodology: it encompasses a sophisticated mathematical process through which the spatial distribution of subsurface physical parameters is reconstructed based on the acquired field measurements. This mathematical reconstruction utilizes iterative algorithms to optimize the fit between the measured data and the calculated response of the proposed subsurface model [33,62].

The precise spatial distribution of resistivity profiles is demarcated by solid red directional indicators, as depicted in Figure 3. The profile lengths were 15.5 m with 0.5 m electrode spacing for the Kepez-1 profile and 21 m with 1.0 m for the Kepez-2 profile. In the Kepez-2 profile, three VES measurements located at the profile's 11th, 12th, and 13th meters were also applied for verification. Two different electrode arrays were utilized for every profile—Wenner Alpha and Wenner–Schlumberger. The "k" parameter represents a dimensionless geometric coefficient that characterizes the spatial relationship between current and potential electrode pairs. Specifically, it quantifies the ratio of the spacing between current and potential electrodes relative to various electrode array configurations. This parameter is fundamental in determining the sensitivity distribution and depth of investigation for different electrode arrangements. Then, the measured resistivity data were inverted by executing the RES2DINV [63] inversion software to obtain the actual resistivity values of the subsurface. The computational algorithm employs a modified conditioned least squares smoothing method, enhanced through implementation of the quasi-Newton optimization technique. The inversion protocol generates a discretized subsurface model composed of rectangular prismatic elements, systematically determining the resistivity distribution through an iterative process. This process optimizes the resistivity values for individual prismatic cells by minimizing the root mean square (RMS) discrepancy between the observed field measurements and the calculated apparent resistivity values. To examine data misfit (D_i), the observed apparent resistivity values ($\varrho_{a(obs)}$) are compared with the calculated resistivity values ($\varrho_{a(cal)}$) at each data point [56] as seen in Equation (8).

$$D_i = \left[\left(\rho_{a(obs)} - \rho_{a(cal)}\right)/\rho_{a(obs)}\right]^2 \cdot 100 \quad (8)$$

RMS is calculated using data misfit for the entire pseudosection, as seen in Equation (9), where *N* is the number of data points.

$$RMS = \left[(1/N)\cdot\left(\sum(D_i)^2\right)\right]^{1/2} \quad (9)$$

The quasi-Newton approach facilitates rapid convergence while maintaining solution stability through appropriate regularization parameters [64,65].

3.4. Data Acquisition and Inversion Parameters

Details of the ERI acquisition geometry, survey configurations, and inversion parameters employed in this study are summarized in Table 1. These parameters define the data acquisition procedure and inversion settings used for the interpretation of the subsurface resistivity models. The inversion employed the default damping factor, automatically adjusted by the software during successive iterations, executed until convergence criteria defined by the software were satisfied. Three Vertical Electrical Sounding (VES) measurements were conducted using a custom-built DC resistivity system configured in the Schlumberger array (Table 2). The soundings were acquired at three locations (11, 12, and 13 m) along the Kepez-2 profile with a maximum current electrode spacing (AB) of 19 m. The acquired VES data were interpreted using one-dimensional inversion in IPI2Win [66], and the resulting layered resistivity models were subsequently imported into Surfer [67] to generate a pseudo-two-dimensional visualization using the minimum-curvature interpolation algorithm.

Table 1. Electrical Resistivity Imaging (ERI) acquisition and inversion parameters.

Parameter	Kepez-1 Profile	Kepez-2 Profile
Instrument	ARES II (GF Instruments, Czech Republic)	
Survey method	Electrical Resistivity Imaging (ERI)	
Electrode configuration	Wenner Alpha and Wenner–Schlumberger	
Number of electrodes [a]	32	22
Electrode spacing [a]	0.5 m	1.0 m
Profile length [a]	15.5 m	21.0 m
Investigation depth [a]	~2.5–3.0 m	~4.0 m
Inversion software	RES2DINV v3.5	
Inversion algorithm	Standard Gauss–Newton least-squares	
Forward modeling	Finite-difference	
Inversion parameter	Logarithm of apparent resistivity	
Regularization	Standard least-squares constraints	
Mesh type	Normal mesh	
Convergence criterion	Relative RMS error change of 5%	

[a] Parameters differ between the profiles because of differences in survey geometry and profile length.

Table 2. Vertical Electrical Sounding (VES) acquisition and interpretation parameters.

Parameter	Kepez-2 Profile
Instrument	Custom-built DC resistivity system
Survey method	Vertical Electrical Sounding (VES)
Survey locations	Three sounding points (11 m, 12 m, and 13 m)
Electrode configuration	Schlumberger
Number of measurements per sounding	10
Maximum current electrode spacing (AB)	19 m (AB/2 = 9.5 m)
Potential electrode spacing (MN)	1–3 m [a]
Maximum resistivity values	6258 (11 m), 4721 (12 m), 4850 (13 m) [ohm.m]
Interpretation software	IPI2Win v3.0.1
Interpretation method	One-dimensional (1-D) inversion
Visualization software	Surfer v10.2.601 (Golden Software, Golden, CO, USA)
Interpolation method	Minimum Curvature

[a] The initial MN spacing varied between 1 and 2 m depending on field conditions, while an MN spacing of 3 m was adopted for larger current electrode separations.

3.5. Vertical Electrical Sounding Interpolation

The interpreted one-dimensional VES models were imported into Surfer [67] to generate a pseudo-two-dimensional visualization of the subsurface resistivity distribution. Lateral resistivity variations between adjacent sounding locations were estimated using the minimum-curvature interpolation algorithm, which provides a smooth representation of spatial resistivity trends while minimizing local surface curvature. This interpolation assumes gradual lateral variations in subsurface resistivity between neighboring VES stations and does not account for abrupt geological discontinuities. Consequently, the resulting pseudo-two-dimensional section is intended solely as a qualitative visualization for comparison with the ERI-derived resistivity models and the observed cavity geometry. It should not be interpreted as a fully constrained two-dimensional geoelectrical inversion model, but rather as an interpolated representation of discrete one-dimensional VESs.

3.6. Inversion Procedure

The apparent resistivity data were inverted using the RES2DINV software [63]. A standard Gauss–Newton least-squares inversion algorithm was employed to obtain the subsurface resistivity models. Forward modeling was performed using the finite-difference method, while the logarithm of the apparent resistivity values was used as the inversion parameter. Standard least-squares constraints are applied to both the model parameters and the measured data to obtain stable inversion models. A normal mesh was adopted, with model cell widths equal to the unit electrode spacing and four finite-element nodes located between adjacent electrodes. Model convergence is controlled using a relative RMS error change criterion of 5% between successive iterations. The inversion process was terminated when the convergence criterion was satisfied or when no significant improvement in the data misfit was achieved.

3.7. Methodological Framework, Detection Capability, and Limitations

The methodological framework adopted in this study was designed to test the hypothesis that shallow air-filled dissolution cavities developed within porous tufa deposits generate sufficient electrical resistivity contrast to be resolved by high-resolution Electrical Resistivity Imaging (ERI). Based on the selected electrode spacing and profile geometry, the survey was optimized for detecting cavities located within the upper approximately 3–4 m of the subsurface. The method is expected to provide the highest detection reliability for air-filled cavities of sufficient lateral extent that produce distinct resistivity contrasts with the surrounding tufa. Conversely, the detection capability decreases for small, deeply buried, water-filled, or sediment-filled cavities because of reduced resistivity contrast and the smoothing effects inherent to inversion algorithms. To mitigate these limitations, ERI interpretations were evaluated together with VES measurements, direct field observations of exposed cavities, and geological evidence, thereby improving the reliability of the interpreted subsurface cavity geometry.

4. Experimental Results

Inversion, Convergence, and Data-Fitting Quality

The quality of the inversion models was evaluated using the root mean square (RMS) error between the measured and calculated apparent resistivity data. RMS error provides a quantitative measure of the data misfit and is commonly used to assess the convergence and reliability of electrical resistivity imaging (ERI) inversion models. Lower RMS values indicate a closer agreement between the observed and calculated datasets and, consequently, a more reliable representation of the subsurface resistivity distribution.

The evolution of RMS error values during successive inversion iterations for both the Wenner Alpha and Wenner–Schlumberger arrays is illustrated in Figure 6. The corresponding RMS error values and percentage reductions for each iteration are presented in Table 3 for the Kepez-1 profile and Table 4 for the Kepez-2 profile. For all datasets, the inversion exhibited rapid convergence during the initial iterations. The most significant reduction in RMS error occurred between the first and second iterations, with error reductions ranging from approximately 60% to 65%, indicating substantial improvement of the initial resistivity model. Subsequent iterations produced progressively smaller decreases in RMS error, demonstrating that the inversion gradually approached a stable solution.

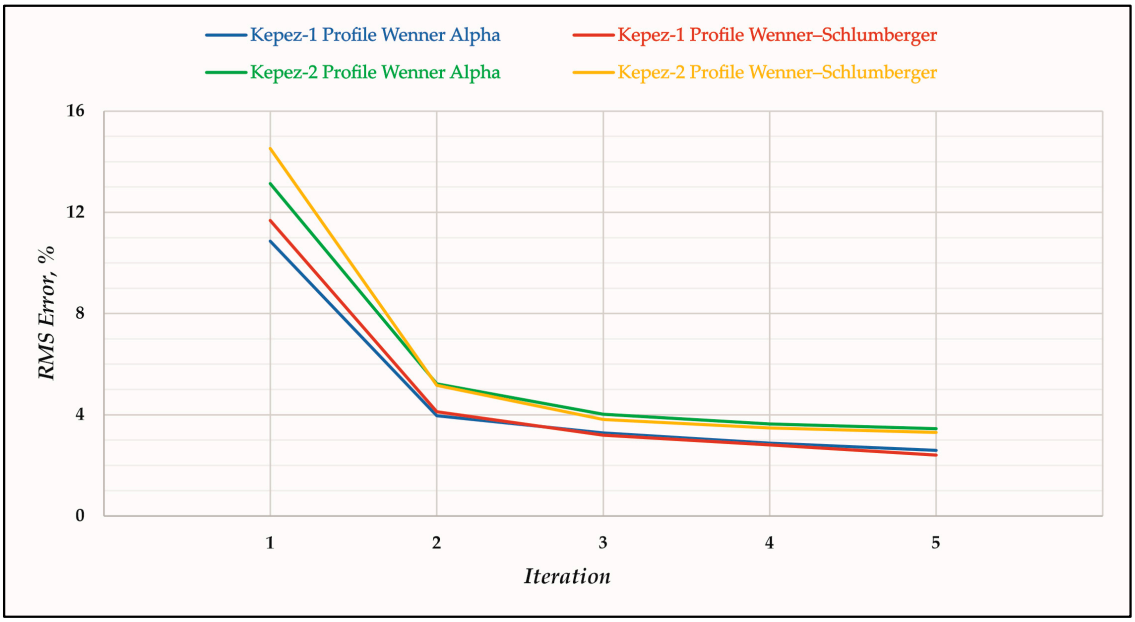

Figure 6. Variation in RMS error values during successive inversion iterations for the Kepez-1 and Kepez-2 profiles using the Wenner Alpha and Wenner–Schlumberger arrays.

Table 3. RMS error values and percentage reduction during successive inversion iterations for the Kepez-1 profile using the Wenner Alpha and Wenner–Schlumberger arrays.

Profile	Kepez-1			
Array	Wenner Alpha		Wenner–Schlumberger	
Iteration	RMS Error (%)	Reduction (%)	RMS Error (%)	Reduction (%)
1	10.867	-	11.676	-
2	3.964	63.523	4.118	64.731
3	3.277	17.331	3.196	22.390
4	2.880	12.115	2.806	12.203
5	2.594 [a]	9.931	2.409 [a]	14.148

[a] Final RMS errors (%) of arrays.

For the Kepez-1 profile, the final RMS errors were 2.594% for the Wenner Alpha array and 2.409% for the Wenner–Schlumberger array. Similarly, the Kepez-2 profile yielded final RMS errors of 3.451% and 3.302% for the Wenner Alpha and Wenner–Schlumberger arrays, respectively. In both profiles, the Wenner–Schlumberger configuration consistently produced slightly lower RMS errors than the Wenner Alpha array, indicating a marginally better agreement between the measured and calculated apparent resistivity data. However, the differences between the two electrode configurations were relatively small, suggest-

ing that both arrays provided comparable inversion performance under the investigated field conditions.

Table 4. RMS error values and percentage reduction during successive inversion iterations for the Kepez-2 profile using the Wenner Alpha and Wenner–Schlumberger arrays.

Profile	Kepez-2			
Array	Wenner Alpha		Wenner–Schlumberger	
Iteration	RMS Error (%)	Reduction (%)	RMS Error (%)	Reduction (%)
1	13.138	-	14.526	-
2	5.218	60.283	5.162	64.464
3	4.015	23.055	3.815	26.095
4	3.636	9.440	3.479	8.807
5	3.451 [a]	5.088	3.302 [a]	5.088

[a] Final RMS errors (%) of arrays.

A comparison between the two survey sites reveals that the Kepez-2 profile consistently yielded higher RMS errors than the Kepez-1 profile, regardless of the electrode configuration. Because this trend was observed for both arrays, the higher misfit is more likely attributable to site-specific subsurface conditions than to differences in the acquisition geometry. Increased geological heterogeneity, including variations in tufa texture, fracture density, moisture distribution, and cavity geometry, may have contributed to the relatively higher inversion misfit observed in the Kepez-2 profile.

Overall, all four inversion models converged successfully after five iterations and achieved final RMS errors below 4%. These results indicate satisfactory agreement between the measured and calculated apparent resistivity data and demonstrate that the inversion process produced stable and reliable resistivity models suitable for interpreting shallow karst cavities within the investigated tufa deposits. Nevertheless, it should be recognized that RMS error alone does not fully quantify model accuracy. The reliability of the interpreted cavity geometry was therefore evaluated together with field observations, exposed cavity geometry, and VES data (at Kepez-2 profile), providing an integrated assessment of the geophysical interpretation.

Figure 6 demonstrates a consistent convergence behavior for all four inversion models. A pronounced reduction in RMS error occurred between the first and second iterations, indicating rapid adjustment of the initial resistivity models to the measured apparent resistivity data. After the third iteration, the convergence curves gradually approached a plateau, with only marginal reductions in RMS error observed during the subsequent iterations. This plateau observed after the third iteration suggests that the inversion had effectively converged and that additional iterations would likely result in only negligible improvements in the data misfit. The absence of oscillations or increases in RMS error indicates stable numerical convergence throughout the inversion process. Furthermore, the Kepez-2 profiles consistently exhibited slightly higher RMS errors than the Kepez-1 profiles, whereas the Wenner–Schlumberger array yielded marginally lower final RMS errors than the Wenner Alpha array for both survey sites. These results demonstrate that all inversion models converged successfully and provided satisfactory data fitting for the investigated karst environment.

The ERI method determined the occurrence of air-filled cavities. After measurement, an inversion process is performed based on an iterative method that attempts to minimize the difference between the calculated and measured apparent resistivity values. Generally, the most reliable model is obtained immediately following the iteration where the root-mean-square (RMS) error shows minimal change (an improvement of

approximately 0.5%). This stabilization typically occurs between the fourth and sixth iterations [68].

The 2D resistivity profiles obtained through the inversion process were subsequently analyzed and interpreted, as demonstrated in Figures 7–11. The displayed resistivity models represent the complete inverted sections for the entire survey profile. The progressive triangular narrowing of the models with depth reflects the natural reduction in data coverage associated with the ERI acquisition geometry, which is an inherent characteristic of the method. The 2D resistivity profile results were systematically compared with the observed morphological characteristics of air-filled cavities to evaluate the correlation accuracy between ERI measurements and the spatial parameters (depth and geometry) of these features. Two distinct electrode array configurations were implemented for each profile, where the designations 'a' and 'b' correspond to the respective array configurations applied to identical profile locations.

The length of the Kepez-1 profile was 15.5 m with a 0.5 m electrode spacing—as illustrated in Figure 7a,b—for different array configurations. The penetration depth for profile 1 was restricted to about 3 m, as it is directly related to the profile length and the spacing of the electrodes. First, 1–1.5 m was interpreted as "competent tufa" due to resistivity values of 900–5000 ohm.m. After 1.5 m depth, the "cavity" occurred up to the deepest point of the section (3 m), with resistivity values of more than 15,000 ohm.m. The Wenner–Schlumberger pseudosection was superimposed on topography in actual scale, and this increase in resistivity values matched closely with the inside cavity roof (Figure 8).

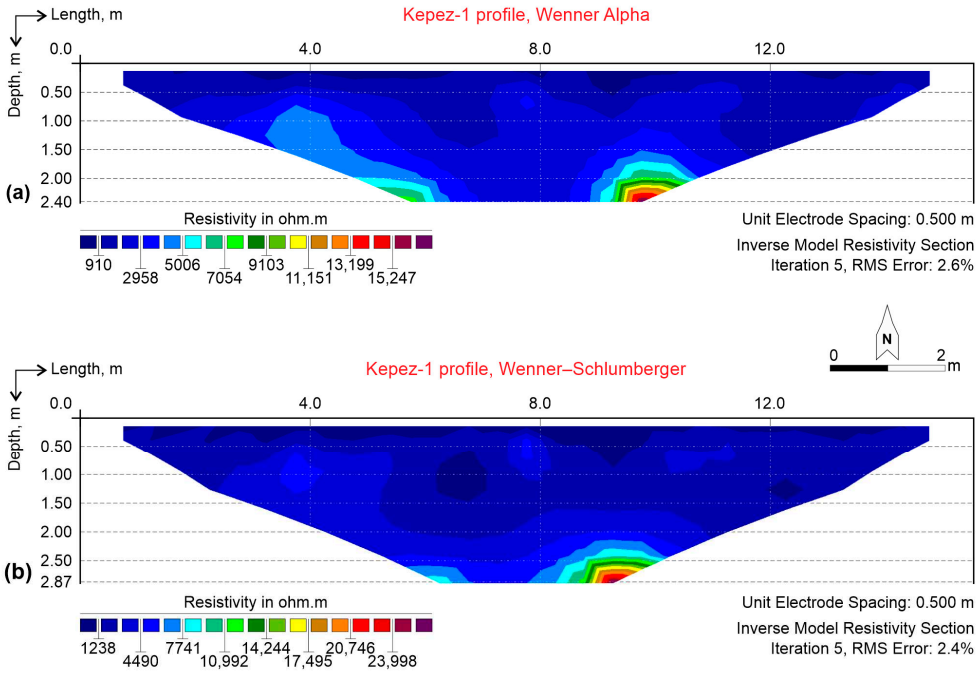

Figure 7. Interpretations of electrode configurations for the Kepez-1 profile: (**a**) interpretation of Wenner Alpha; (**b**) interpretation of Wenner–Schlumberger (displayed resistivity models correspond to the full survey line).

Figure 9 illustrates the 2D resistivity image for the Kepez-2 profile. The profile length was 21 m, and the reachable depth was about 4 m. The first 1–1.5 m depth was occupied by "competent tufa", with resistivity values of 900–5000 ohm.m. This part (1–1.5 m) was underlain by a "cavity" with high resistivity values (more than 13,000 ohm.m).

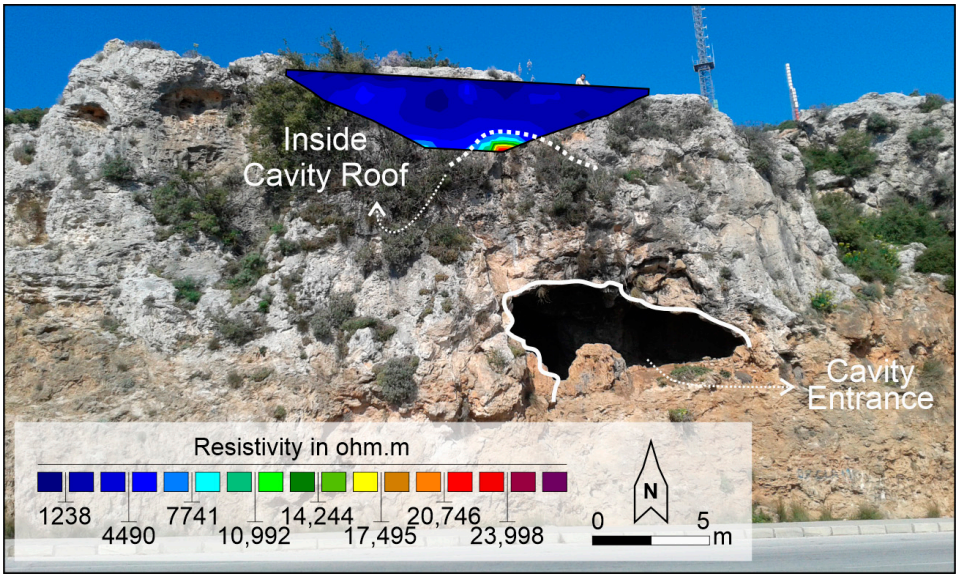

Figure 8. View of the Kepez-1 profile with topographic section. Inversion model reveals a well-defined high-resistivity anomaly at approximately 9.5 m along the profile and 2.3 m depth, which is interpreted as the upper boundary (roof) of an air-filled karst cavity developed within the limestone bedrock.

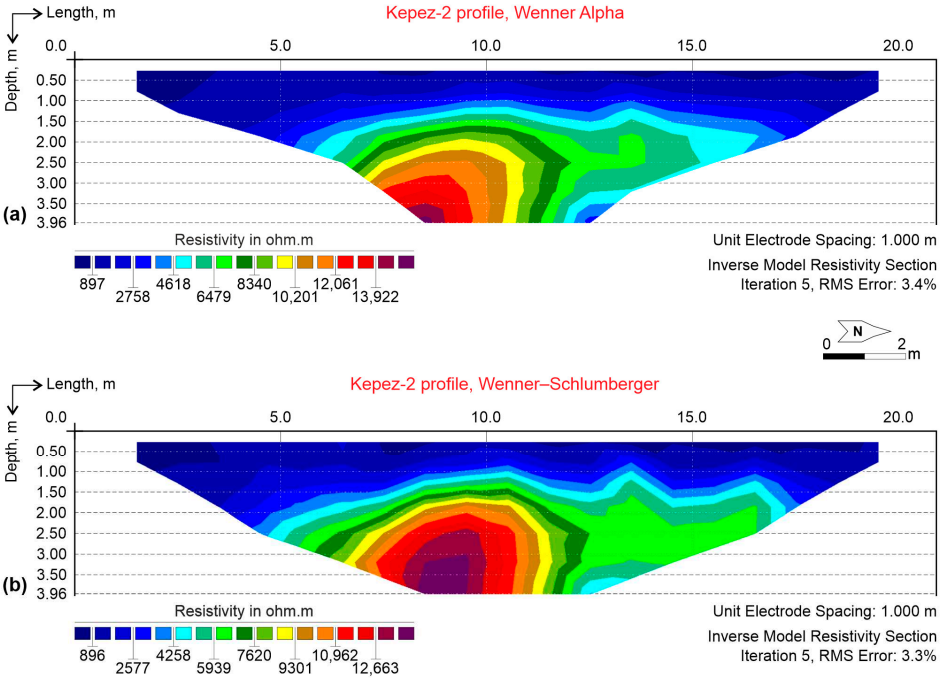

Figure 9. Interpretations of electrode configurations for the Kepez-2 profile: (**a**) interpretation of Wenner Alpha; (**b**) interpretation of Wenner–Schlumberger (displayed resistivity model corresponds to the full survey line).

The VES analyses at the Kepez-2 profile were applied at 3 points (11th, 12th, and 13th meters of the ERI profile). At those points, the observed resistivity values of ERI (Figure 10a) and VES (Figure 10b) were examined separately, and the two datasets matched well (Figure 10c). It is a fact that three individual vertical-sounding images acquired from VES analyses, where the distance between the A and B electrodes is 18 m. Those resistivity images were interpolated to gain one resistivity image like ERI (Figure 10b).

The cavity that exists in the Kepez-2 region has a clearer view than that of the Kepez-1 region, as seen in Figure 11a. The inverted resistivity section of Wenner–Schlumberger method was superimposed on the topography, and the cavity roof is in good agreement

with the interpretation of the Kepez-2 profile resistivity values (Figure 11b). Similarly, the resistivity values obtained by VES were transferred to 2D by utilizing IPI2WIN [66] software [69]; these are also compatible with the visual occurrence of the cavity roof (Figure 11c).

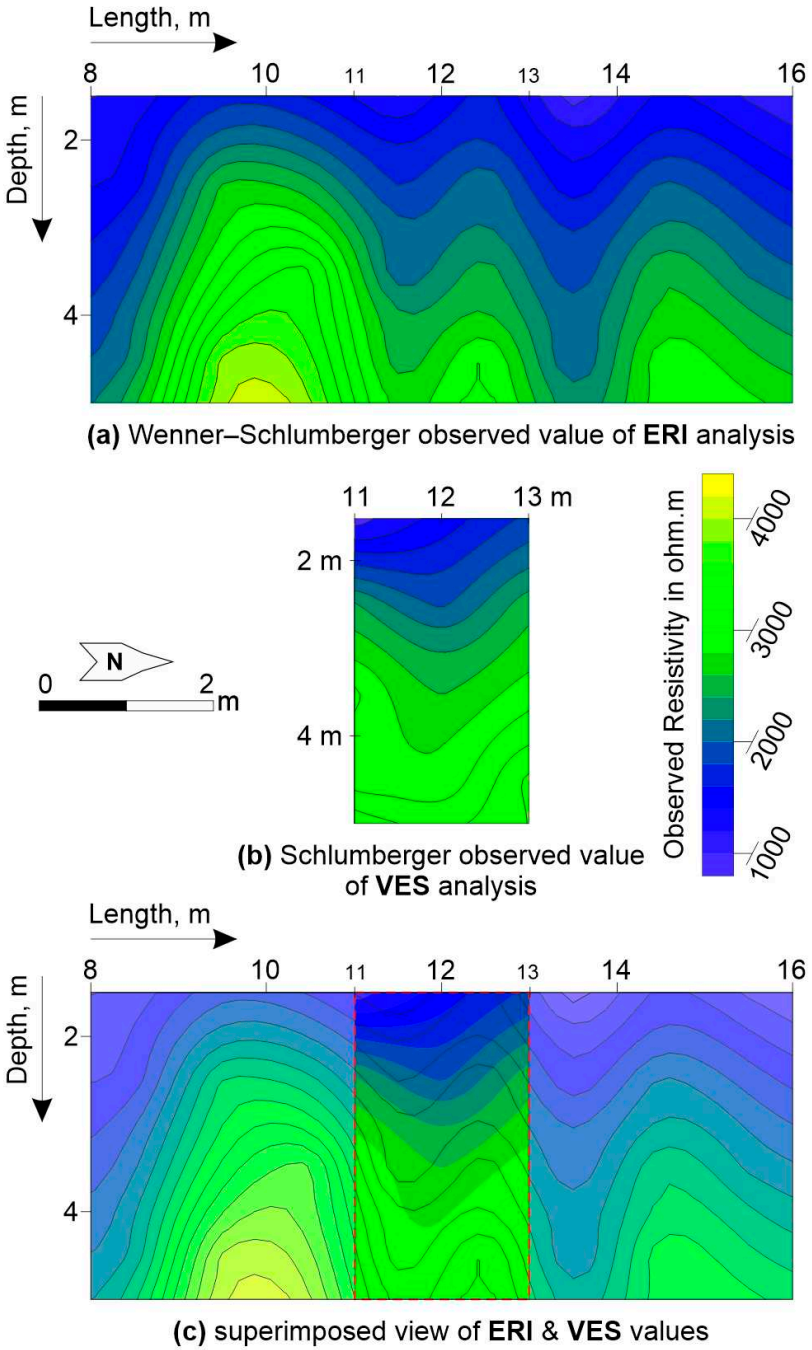

Figure 10. (**a**) Wenner–Schlumberger observed value of ERI for Kepez-2 profile; (**b**) Schlumberger observed value of VES for Kepez-2 profile; (**c**) superimposed view of ERI and VES values for Kepez-2 profile (rectangle surrounded by dashed red lines, including the ERI values shown with black lines and the VES values with colored zones).

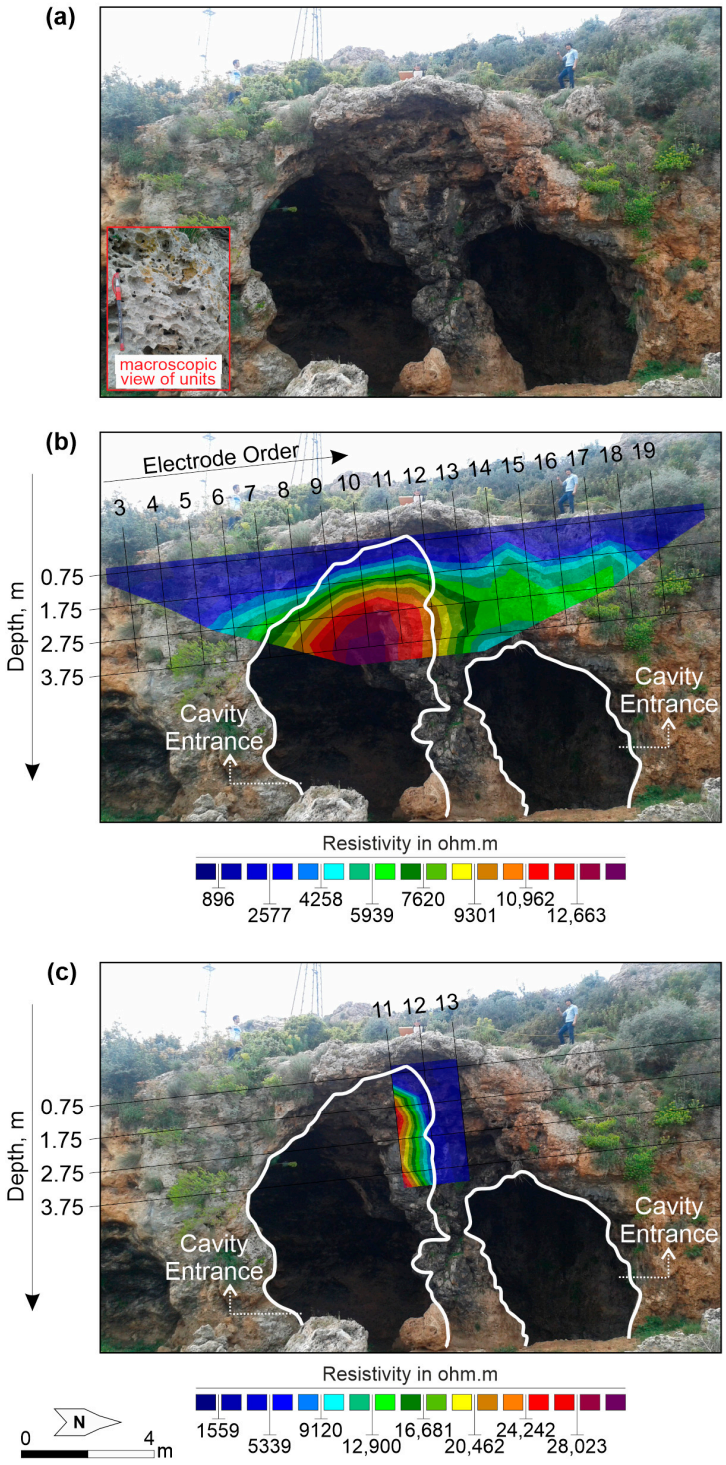

Figure 11. View of the Kepez-2 profile: (**a**) topographical section for Kepez-2 profile; (**b**) superimposed view of ERI with topographical section for Kepez-2 profile; (**c**) superimposed view of VES with topographical section for Kepez-2 profile.

5. Discussion

Among the available geophysical techniques (Table 5), ERI was considered the most appropriate method for the investigated Antalya tufa deposits because the target cavities were shallow, predominantly air-filled, and characterized by high electrical resistivity contrasts with the surrounding host material. Although ground-penetrating radar (GPR) can provide higher near-surface resolution under dry conditions, its performance may be

significantly reduced in conductive or moisture-rich materials. Microgravity and seismic refraction are valuable complementary techniques, particularly for detecting larger or deeper subsurface voids; however, they generally provide lower spatial resolution for small karst cavities than ERI. The integration of ERI with VES in the present study improved the reliability of subsurface interpretation by combining continuous two-dimensional resistivity imaging with localized one-dimensional depth verification.

Table 5. Comparison of commonly used geophysical methods for karst cavity detection and their applicability to the investigated Antalya tufa deposits.

Method	Detection Principle	Main Advantages	Main Limitations	Suitability for Antalya Tufa
ERI	Electrical Resistivity Contrast	High sensitivity to air-filled cavities, non-destructive, continuous 2D imaging, and relatively low cost	Resolution decreases with depth; influenced by groundwater saturation and cavity infill	High
GPR	Electromagnetic Wave Reflection	Very high near-surface resolution, rapid data acquisition	Limited penetration in conductive or moist materials; signal attenuation	Moderate–High (dry conditions)
Microgravity	Density Contrast	Effective for detecting large underground voids	Low resolution for small cavities; sensitive to environmental noise; requires precise elevation control	Moderate
Seismic	Seismic Velocity Contrast	Provides mechanical information and bedrock geometry	Poor sensitivity to small air-filled cavities; interpretation may be ambiguous in heterogeneous materials	Moderate
ERI + VES (this study)	Combined Electrical Methods	Improved confidence through complementary 2D imaging and 1D depth verification	Limited investigation depth in short profiles	High

The bulk resistivity of tufa deposits is controlled by several interrelated geological and hydrogeological factors, including water saturation, air saturation, porosity, and mineral composition. Among these, water saturation exerts the strongest influence because increasing groundwater content enhances electrical conductivity and significantly reduces bulk resistivity. In contrast, air-filled pores and cavities increase the resistivity contrast with the surrounding host material, making them more readily detectable by Electrical Resistivity Imaging (ERI). The effect of porosity depends largely on the nature of the pore-filling material. High-porosity tufa saturated with groundwater generally exhibits relatively low resistivity values, whereas highly porous but air-filled tufa produces significantly higher resistivity. In addition, although the investigated tufa deposits consist predominantly of calcite, the presence of clay minerals, iron oxides, or secondary mineral infillings may locally modify the electrical properties by reducing or increasing the bulk resistivity. Consequently, the interpretation of resistivity anomalies should always consider the combined influence of lithology, pore-fluid characteristics, and hydrogeological conditions rather than resistivity values alone.

The selection of the electrode array influences the spatial resolution, depth of investigation, and sensitivity to subsurface resistivity variations. Although Dipole–Dipole arrays are generally recognized for providing higher lateral resolution, they are more susceptible to noise and typically exhibit lower signal strength. In contrast, the Wenner Alpha and Wenner–Schlumberger arrays employed in this study provided stable inversion results and sufficient investigation depth for the delineation of shallow air-filled cavities within the Antalya tufa deposits. Nevertheless, the influence of alternative electrode arrays on the detection of shallow karst cavities under different geological and hydrogeological conditions warrants further investigation. In the present study, the Wenner–Schlumberger

array consistently produced slightly lower final RMS errors than the Wenner Alpha array, indicating a marginally improved data fit under the investigated field conditions. The potential influence of array selection on cavity imaging should be systematically evaluated in future studies.

Because the resistivity models were generated using a smoothness-constrained inversion algorithm, the interpreted resistivity anomalies appear smoother and laterally more extensive than the actual cavity geometry. Consequently, the boundaries of individual cavities should be regarded as approximate rather than exact representations of their true dimensions. This effect is an inherent characteristic of least-squares inversion and should be considered when interpreting the geometry of shallow karst cavities.

Quantitative comparison of cavity dimensions was not possible because accurate geometric measurements of the exposed cavities were unavailable. Therefore, the comparison between the inverted resistivity models and field observations was performed qualitatively, focusing on the spatial correspondence between the interpreted anomalies and the exposed karst cavities.

The effectiveness of Electrical Resistivity Imaging (ERI) for detecting subsurface karst cavities is primarily controlled by the magnitude of the electrical resistivity contrast between the cavity and the surrounding host rock. Among the controlling factors, groundwater saturation exerts the greatest influence because it significantly decreases the bulk resistivity of the subsurface, making water-filled cavities more difficult to distinguish from the surrounding rock. In contrast, air-filled cavities generally produce the highest resistivity contrast and therefore represent the most favorable targets for ERI investigations, whereas cavities partially or completely filled with clay-rich sediments exhibit relatively low resistivity values, reducing the resistivity contrast and increasing interpretation uncertainty. Additional factors, including pore-water conductivity, moisture content, seasonal groundwater-level fluctuations, temperature, and local hydrogeological conditions, may further modify the electrical properties of both the host rock and cavity fillings. In the investigations of Antalya tufa deposits, the verified cavities were predominantly air-filled and generated sufficiently high resistivity contrasts to permit reliable delineation of shallow dissolution features. Accordingly, the successful application of ERI in this study reflects the favorable geological and hydrogeological conditions of the investigated site and should not be interpreted as representing a universally applicable resistivity response for all karst environments. Rather, the applicability of ERI should always be evaluated within the geological and hydrogeological framework of each study area.

In addition to cavity infill, several environmental and geological factors may influence resistivity measurements. Variations in pore-water conductivity, seasonal groundwater-level fluctuations, and, to a lesser extent, temperature can modify the electrical properties of both the host rock and cavity fillings. Therefore, the detectability of karst cavities should always be evaluated within the local geological and hydrogeological framework rather than assuming a universal resistivity response.

The cavities investigated in this study were predominantly air-filled and developed within highly porous tufa deposits under the prevailing hydrogeological conditions of the Antalya Basin. Under these conditions, sufficiently high resistivity contrasts were generated to permit reliable delineation of the cavities using ERI. Accordingly, the conclusions of this study should be interpreted as being representative of the investigated site conditions rather than universally applicable to all karst environments.

The progressive reduction in RMS error demonstrates stable model convergence. Subsequent iterations produced only minor improvements, indicating that the inversion had reached a stable solution. Final RMS errors below 5% suggest a good fit between the observed and calculated apparent resistivity data and support the robustness of the

interpreted resistivity models. Therefore, the adopted models are considered to provide a reliable representation of the shallow resistivity structure within the limitations of the inversion algorithm.

Based on the ERI responses observed in this study, a preliminary engineering risk classification is proposed for shallow karst cavities developed within the Antalya tufa deposits (Table 6). The classification is intended to provide a practical framework for interpreting resistivity anomalies during preliminary site investigations rather than a universally applicable engineering standard. Final engineering decisions should always be supported by site-specific geological observations, geotechnical investigations, and, where appropriate, confirmatory drilling.

Table 6. Proposed engineering risk classification based on ERI anomaly characteristics in the Antalya tufa deposits.

Risk Level	ERI Characteristics	Interpretation	Recommended Engineering Action	Risk Level
Low	No significant resistivity anomaly	Intact tufa with no evidence of cavity development	Standard foundation design	Low
Moderate	Localized high-resistivity anomaly with limited lateral extent	Possible small air-filled cavity or dissolution zone	Detailed site investigation and verification drilling, if required	Moderate
High	Well-defined high-resistivity anomaly with continuous lateral extent	Probable air-filled karst cavity	Avoid shallow foundations or perform ground improvement before construction	High
Very High	Large, continuous high-resistivity anomaly associated with surface deformation or exposed cavities	Confirmed or highly probable karst cavity with collapse potential	Detailed geotechnical investigation, cavity treatment, or redesign of engineering structures	Very High

The proposed workflow is intended for shallow engineering investigations and should not be interpreted as a replacement for deep geophysical exploration targeting mature karst systems. Air-filled cavities represent the highest resistivity contrast and therefore constitute the most favorable target for ERI. Water-filled or sediment-filled cavities are expected to exhibit substantially lower resistivity contrasts, making their identification more challenging. The objective of this study was to evaluate the capability of ERI to delineate known shallow dissolution cavities rather than to assess survey repeatability.

Although the high-resistivity anomalies correspond well with the observed air-filled cavities, the limited number of directly verified cavities does not allow the establishment of a statistically robust relationship among cavity size, burial depth, and resistivity magnitude. Therefore, the relationship was evaluated semi-quantitatively by comparing the spatial correspondence between the observed cavities and the interpreted high-resistivity zones. It should also be noted that smoothness-constrained inversion and current diffusion tend to broaden sharp resistivity contrasts; therefore, the interpreted anomaly boundaries should be regarded as approximate indicators of cavity location rather than exact representations of cavity geometry.

Beyond the identification of subsurface cavities, geophysical investigations contribute to engineering decision-making by supporting hazard assessment, land-use planning, and

the sustainable development of karst-prone regions. Therefore, the reliable delineation of shallow karst features represents an important prerequisite for reducing geotechnical uncertainty during site characterization [30].

To integrate the geological observations with the geophysical interpretation, a conceptual model of karst cavity evolution and its corresponding ERI response is proposed (Figure 12). The model summarizes the inferred sequence of hydrogeological and karstification processes leading to cavity formation, roof instability, sinkhole development, and the associated resistivity anomalies observed in the present study. The conceptual model is intended to provide a generalized representation of the dominant karstification processes inferred from the field observations and geophysical results obtained in this study. It emphasizes the hydrogeological controls governing cavity development and highlights the progressive relationship between cavity evolution and the corresponding ERI response. Although the model is based on the Antalya tufa deposits, the overall conceptual framework may also be applicable to similar shallow tufa karst environments. The proposed conceptual model integrates the geological observations, hydrogeological processes, and geophysical interpretation obtained in this study, providing a framework for understanding sinkhole development and its engineering implications in shallow tufa karst environments.

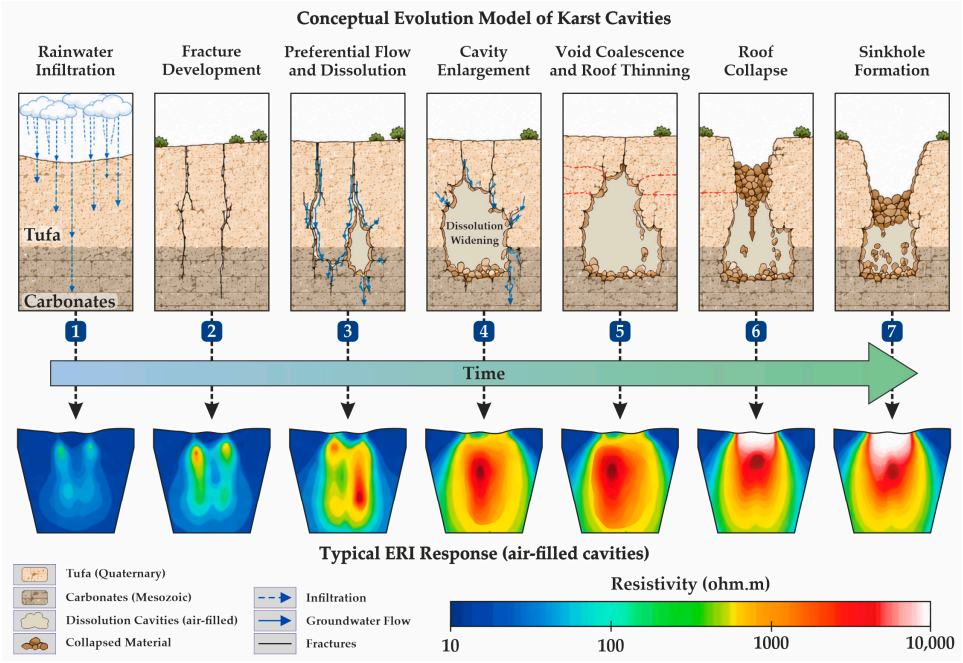

Figure 12. Proposed conceptual model illustrating the evolution of shallow air-filled karst cavities and their corresponding ERI response in the tufa deposits. (1) Rainwater infiltrates into the highly porous tufa deposits; (2) tectonic uplift and diagenetic processes generate fractures, increasing secondary permeability; (3) slightly acidic groundwater migrates along preferential flow paths, initiating carbonate dissolution and enlarging fractures into small solution cavities; (4) progressive dissolution promotes both lateral and upward cavity enlargement through continued removal of carbonate material; (5) adjacent cavities coalesce, leading to progressive roof thinning and reduced structural stability; (6) once the residual roof strength falls below the overburden stress, collapse is initiated; (7) repeated collapse and continued dissolution ultimately result in sinkhole formation at the ground surface, with the potential for further reactivation over time.

Neither geophysical nor geotechnical methods alone are sufficient for comprehensive karst characterization. ERI provides continuous subsurface imaging and efficiently identifies potential cavity zones; however, because it is an indirect method, the interpretation should be verified using direct geological information whenever possible. Borehole investigations provide definitive confirmation of subsurface conditions but are limited to

discrete locations and may fail to intersect localized cavities. Therefore, integrating ERI with targeted borehole investigations represents the most reliable strategy for engineering-scale characterization of shallow karst terrains, reducing interpretation uncertainty while optimizing investigation costs (Table 7). Although ERI cannot replace direct subsurface verification by borehole investigations, it provides a reliable basis for selecting optimal drilling locations. Consequently, integrating ERI with targeted boreholes minimizes geological uncertainty, reduces unnecessary drilling, and improves the cost-effectiveness of engineering site investigations. Accordingly, ERI should be considered as a complementary investigation method rather than a replacement for borehole drilling. The integration of both methods provides the highest level of confidence for the detection and characterization of shallow karst cavities in engineering practice.

Table 7. Comparison of commonly used investigation methods for engineering-scale assessment of shallow karst cavities.

Method	Advantages	Limitations	Recommended Application
ERI	Rapid, non-destructive, provides continuous two-dimensional subsurface imaging, effective for identifying high-resistivity anomaly zones associated with air-filled cavities	Indirect method; interpretation should be validated using geological or geotechnical data	Preliminary site investigation, cavity detection, and engineering risk mapping
Borehole	Provides direct geological and geotechnical information and confirms cavity presence	Point-based investigation, relatively expensive, and may miss cavities located between boreholes	Verification of critical geophysical anomalies and detailed site characterization
Integrated ERI and Borehole	Combines continuous subsurface imaging with direct ground truth, significantly reducing interpretation uncertainty	Requires coordinated survey planning and higher investigation costs	Comprehensive engineering site characterization, geotechnical design, and hazard assessment

6. Conclusions

As shown in Figures 7 and 9, the shape of the contours in the inverted resistivity section produced by the different arrays over the same structure can differ. Selecting the optimal array for a field survey depends on the type of structure being mapped, the sensitivity of the resistivity meter, and the level of background noise. The key characteristics of an array that require consideration include the investigation depth, array sensitivity to both vertical and horizontal subsurface resistivity variations, horizontal data coverage extent, and signal strength magnitude. The Wenner Alpha array demonstrates optimal performance in noise-contaminated environments due to its superior signal strength, while simultaneously providing enhanced vertical resolution capabilities. The Wenner–Schlumberger array configuration, incorporating overlapping data levels, presents a viable methodology when concurrent horizontal and vertical resolution optimization is required, particularly in scenarios demanding robust signal strength.

The electrical methods (ERI and VES) are conducted by spreading current in the subsurface; therefore, their performance can be affected by factors like water content, temperature, metal content, porosity, permeability, etc., that affect the movement of current. The electrical methods give better results if there is a sufficient contrast in the subsurface material properties regarding resistivity, as in this study.

It is imperative to emphasize that the aforementioned interpretations are inherently site-specific and should be evaluated within their respective geological contexts. For example, resistivity values of 900–5000 ohm.m were attributed to "competent tufa" since the profile cross-section is clearly seen. Similarly, visual appearances of air-filled cavities supplied clues about corresponding resistivity values of 13,000 ohm.m–15,000 ohm.m for both profiles. Furthermore, the contribution of the VES method cannot be ignored, especially for interpreting the Kepez-2 profile.

The successful delineation of air-filled karst cavities by ERI in this study reflects the favorable resistivity contrast generated under the prevailing geological and hydrogeological conditions of the investigated Antalya tufa deposits. The applicability of this approach to other karst settings should be evaluated with consideration of cavity filling, groundwater conditions, and other factors influencing subsurface resistivity.

The inverted ERI models (mentioned as pseudosections) show the main rock (carbonates) with a significantly lower resistivity than the cavities (Figures 7 and 9). This high contrast in electrical resistivity values between carbonate rock and cavities makes it possible to use ERI to determine the subsurface structure. To conclude, ERI is an easily applied method that accurately acquires resistivity data. It is very capable of detecting subsurface cavities, especially in karstic terrains. Due to the sharp contrast of cavities with their environment, the depth and geometry of different-sized cavities can be easily delineated by utilizing the ERI method. This evaluation technique can be successfully used in other karst areas and may help identify hidden voids and cavities that could create karst hazards. Although only three VES locations were acquired, they were positioned directly over representative ERI anomalies to provide qualitative verification of the interpreted resistivity structure rather than complete subsurface characterization. VES was not intended as an independent regional sounding survey but rather as a local verification tool for the interpreted ERI anomalies. The maximum AB spacing was selected according to site dimensions and the expected depth of the shallow dissolution features. Future investigations should incorporate denser VES coverage and larger electrode spacings to improve the characterization of deeper karst structures. The presented methodology is applicable primarily to shallow air-filled dissolution cavities developed within tufa deposits and should be complemented by deeper investigations where medium- to deep-seated karstification is expected. This survey configuration was optimized for detecting shallow dissolution cavities rather than regional karst architecture.

Author Contributions: Conceptualization, F.U. and Ö.A.; methodology, F.U. and Ö.A.; software, F.U. and Ö.A.; validation, F.U. and Ö.A.; formal analysis, F.U. and Ö.A.; investigation, F.U. and Ö.A.; resources, F.U. and Ö.A.; data curation, F.U. and Ö.A.; writing—original draft preparation, F.U. and Ö.A.; writing—review and editing, F.U. and Ö.A.; visualization, F.U. and Ö.A.; supervision, Ö.A.; project administration, F.U. and Ö.A.; funding acquisition, Ö.A. All authors have read and agreed to the published version of the manuscript.

Funding: This research was funded by the Scientific Research Development Program at Akdeniz University, grant numbers 2013.01.0102.002 and 2013.02.0121.017.

Data Availability Statement: The data presented in this study are available from the corresponding author upon reasonable request.

Conflicts of Interest: The authors declare no conflicts of interest.

Abbreviations

The following abbreviations are used in this manuscript:

ERI	Electrical Resistivity Imaging
RMS	Root Mean Square
VES	Vertical Electrical Sounding

References

1. Martínez-Moreno, F.J.; Pedrera, A.; Ruano, P.; Galindo-Zaldívar, J.; Martos-Rosillo, S.; González-Castillo, L.; Sánchez-Úbeda, J.P.; Marín-Lechado, C. Combined Microgravity, Electrical Resistivity Tomography and Induced Polarization to Detect Deeply Buried Caves: Algaidilla Cave (Southern Spain). *Eng. Geol.* **2013**, *162*, 67–78. [CrossRef]
2. Amanatidou, E.; Vargemezis, G.; Tsourlos, P. Combined Application of Seismic and Electrical Geophysical Methods for Karst Cavities Detection: A Case Study at the Campus of the New University of Western Macedonia, Kozani, Greece. *J. Appl. Geophys.* **2022**, *196*, 104499. [CrossRef]
3. Sowers, G.F. *Building on Sinkholes: Design and Construction of Foundations in Karst Terrain*; ASCE Press: New York, NY, USA, 1996; p. 202.
4. Drumm, E.C.; Aktürk, Ö.; Akgün, H.; Tutluoğlu, L. Stability Charts for the Collapse of Residual Soil in Karst. *J. Geotech. Geoenviron. Eng.* **2009**, *135*, 925–931. [CrossRef]
5. Çiner, A.; Karabıyıkoğlu, M.; Monod, O.; Deynoux, M.; Tuzcu, S. Late Cenozoic Sedimentary Evolution of the Antalya Basin, Southern Turkey. *Turk. J. Earth Sci.* **2008**, *17*, 1–41.
6. Robertson, A.H.F. Mesozoic–Tertiary Sedimentary and Tectonic Evolution of Neotethyan Carbonate Platforms, Margins and Small Ocean Basins in the Antalya Complex of Southwest Turkey. In *Tectonic Controls and Signatures in Sedimentary Successions*; Frostick, L.E., Ed.; John Wiley & Sons: Hoboken, NJ, USA, 1994; pp. 415–465.
7. Dipova, N.; Doyuran, V. Assessment of the Collapse Mechanisms of Tufa Deposits. *Eng. Geol.* **2006**, *83*, 332–342. [CrossRef]
8. Palmer, D. Can New Acquisition Methods Improve Signal-to-Noise Ratios with Seismic Refraction Techniques? *Explor. Geophys.* **2000**, *31*, 275–280. [CrossRef]
9. Koşun, E.; Sarıgül, A.; Varol, B. Lithofacies Properties of Antalya Tufas. *Bull. Miner. Res. Explor.* **2005**, *130*, 57–70.
10. Türker, A.E.; Keçeli, D.A.; Kamacı, Z.; Kaya, M.A. The Ground Problem s of Urban Area in Antalya and Their Resolutions by Means of Gephysical Methods. *Jeofizik* **1991**, *5*, 27–42.
11. Terzaghi, K. *Theoretical Soil Mechanics*; John Wiley and Sons: New York, NY, USA, 1943; p. 510.
12. Moore, H.L. Recent Sinkhole Occurrences Along Highways in East Tennessee, a Historical Perspective. In Proceedings of the 54th Annual Highway Geology Symposium, Burlington, VT, USA, 24–26 September 2003; pp. 46–55.
13. Moore, H.L. A Proactive Approach to Planning and Designing Highways in East Tennessee Karst. *Environ. Eng. Geosci.* **2006**, *12*, 147–160. [CrossRef]
14. Bell, F.G. Subsidence Associated with the Abstraction of Fluids. *Geol. Soc. Lond. Eng. Geol. Spec. Publ.* **1988**, *5*, 363–376. [CrossRef]
15. Tharp, T.M. Mechanics of Upward Propagation of Cover-Collapse Sinkholes. *Eng. Geol.* **1999**, *52*, 23–33. [CrossRef]
16. Kannan, R.C. Designing Foundations Around Sinkholes. *Eng. Geol.* **1999**, *52*, 75–82. [CrossRef]
17. Martin, A.D. Case History of the South Street Sinkhole Frederick, Maryland. In Proceedings of the 55th Annual Highway Geology Symposium, Kansas City, MO, USA, 7–10 September 2004; pp. 81–93.
18. Zhou, W.; Beck, B.F.; Adams, A.L. Application of Matrix Analysis in Delineating Sinkhole Risk Areas Along Highway (I-70 near Frederick, Maryland). *Environ. Geol.* **2003**, *44*, 834–842. [CrossRef]
19. Yang, M.Z.; Drumm, E.C. Stability Evaluation for the Siting of Municipal Landfills in Karst. *Eng. Geol.* **2002**, *65*, 185–195. [CrossRef]
20. Newton, J.G.; Tanner, J.M. *Regional Inventory of Karst Activity in the Valley and Ridge Province, Eastern Tennessee: Phase 1*; Oak Ridge National Laboratory: Oak Ridge, TN, USA, 1987.
21. Glover, C.; Robertson, A.H.F. Origin of Tufa (Cool-Water Carbonate) and Related Terraces in the Antalya Area, SW Turkey. *Geol. J.* **2003**, *38*, 329–358. [CrossRef]
22. Dipova, N.; Doyuran, V. Characterization of the Antalya (Turkey) Tufa Deposits. *Carbonates Evaporites* **2006**, *21*, 144–160. [CrossRef]
23. Dipova, N. Geotechnical Characterization and Facies Change Detection of the Bogacay Coastal Plain (Antalya, Turkey) Soils. *Environ. Earth Sci.* **2010**, *62*, 883–896. [CrossRef]
24. Koşun, E.; Varol, B.; Taşkıran, H. The Antalya Tufas: Landscapes, Morphologies, Age, Formation Processes and Early Human Activities. In *Landscapes and Landforms of Turkey*; Kuzucuoğlu, C., Çiner, A., Kazancı, N., Migon, P., Eds.; World Geomorphological Landscapes; Springer Nature: Cham, Switzerland, 2019; pp. 207–218.

25. Koşun, E. Facies Characteristics and Depositional Environments of Quaternary Tufa Deposits, Antalya, SW Turkey. *Carbonates Evaporites* **2012**, *27*, 269–289. [CrossRef]
26. Nie, F.; Zhang, X.; Zhou, L.; Wang, H.; Hua, J.; Liu, B.; Feng, B. Investigation of Fracture Characteristics and Energy Evolution Laws of Model Tunnels with Different Shapes Subjected to Impact Load. *Materials* **2025**, *18*, 889. [CrossRef] [PubMed]
27. Boluk, H.; Afsin, M.; Kavurmaci, M.M.; Akın, M. Investigation of sinkholes in Kozaklı (Nevşehir) geothermal field usinggeophysical methods. *Niğde Ömer Halisdemir Univ. J. Eng. Sci.* **2022**, *11*, 1074–1084. [CrossRef]
28. Boluk, H.; Afsin, M.; Kavurmaci, M.M.; Akın, M. Geothermal fluid–rock interaction and its impact on physicomechanical behavior: Evidence from in-situ sinkhole exposure experiments. *Carbonates Evaporites* **2026**, *41*, 79. [CrossRef]
29. El Hameedy, M.A.; Mabrouk, W.M.; Dahroug, S.; Metwally, A.M. Detection of karst features and associated geohazard using ground penetrating radar and 2D electrical resistivity imaging; case study from Sannur protectorate, Egypt. *Contrib. Geophys. Geod.* **2023**, *53*, 167–190. [CrossRef]
30. Hitouri, S.; Toto, E.A.; Hafid, M.; Rezouki, I. Application of electrical resistivity tomography to karst Hazard assessment in Azilal (Central High Atlas, Morocco). *J. Afr. Earth Sci.* **2026**, *242*, 106226. [CrossRef]
31. Barbolla, D.F.; Torre, C.; De Giorgi, L.; Leucci, G. New data about Grotta delle Veneri by GPR and ERT surveys. *Digit. Appl. Archaeol. Cult. Herit.* **2026**, *42*, e00560. [CrossRef]
32. Ford, T.D.; Pedley, H.M. A Review of Tufa and Travertine Deposits of the World. *Earth-Sci. Rev.* **1996**, *41*, 117–175. [CrossRef]
33. Reynolds, J.M. *An Introduction to Applied and Environmental Geophysics*, 2nd ed.; Wiley-Blackwell: Chichester, UK, 2011; p. 710.
34. Aktürk, Ö.; Doyuran, V. Integration of Electrical Resistivity Imaging (ERI) and Ground Penetrating Radar (GPR) Methods to Identify Soil Profile Around Necatibey Subway Station, Ankara, Turkey. *Environ. Earth Sci.* **2015**, *74*, 2197–2208. [CrossRef]
35. Aktürk, Ö.; Doyuran, V. Soil Profile Identification Around Necatibey Subway Station (Ankara, Turkey), Using Electrical Resistivity Imaging (ERI). *Int. J. Eng. Appl. Sci.* **2012**, *4*, 1–14.
36. McCrackin, C.; Kiflu, H.; Kruse, S.; van Beynen, P.; Polk, J.; Miller, B. 3D Resistivity Survey Over Mapped Caves in Eogenetic Karst Terrane, West-Central Florida, USA. *J. Cave Karst Stud.* **2022**, *84*, 1–13. [CrossRef]
37. Cardarelli, E.; Cercato, M.; Cerreto, A.; Di Filippo, G. Electrical resistivity and seismic refraction tomography to detect buried cavities. *Geophys. Prospect.* **2010**, *58*, 685–695. [CrossRef]
38. Martines-López, J.; Rey, J.; Dueñas, J.; Hidalgo, C.; Benavente, J. Electrical Tomography Applied to the Detection of Subsurface Cavities. *J. Cave Karst Stud.* **2013**, *75*, 28–37. [CrossRef]
39. Land, L.; Rinehart, A. Geophysical Surveys of a Potentially Extensive Cave System, Guadalupe Mountains, New Mexico, USA. *J. Cave Karst Stud.* **2018**, *80*, 109–120. [CrossRef]
40. Loke, M.H. *Tutorial: 2-D and 3-D Electrical Imaging Surveys, Geotomo Software Lecture Notes; Copyright (1996–2015)*; Geotomo Software, LLC: Houston, TX, USA, 2015; p. 176.
41. Cardarelli, E.; Di Filippo, G. Integrated Geophysical Methods for the Characterization of an Archaeological Site (Massenzio Basilica—Roman forum, Rome, Italy). *J. Appl. Geophys.* **2009**, *68*, 508–521. [CrossRef]
42. Stan, D.; Stan-Kłeczek, I. Application of Electrical Resistivity Tomography to Map Lithological Differences and Subsurface Structures (Eastern Sudetes, Czech Republic). *Geomorphology* **2014**, *221*, 113–123. [CrossRef]
43. Uçar, F.; Aktürk, Ö. Investigation of Similarity Between Electrical Resistivity Results (VES and ERI) at Karstic Regions, Antalya, Turkey. In Proceedings of the 9th International Symposium on Eastern Mediterranean Geology, Antalya, Türkiye, 7–11 May 2018; pp. 120–127.
44. Wise, D.J.; Cassidy, J.; Locke, C.A. Geophysical Imaging of the Quaternary Wairoa North Fault, New Zealand: A Case Study. *J. Appl. Geophys.* **2003**, *53*, 1–16. [CrossRef]
45. Zarroca, M.; Bach, J.; Linares, R.; Pellicer, X.M. Electrical Methods (VES and ERT) for Identifying, Mapping and Monitoring Different Saline Domains in a Coastal Plain Region (Alt Empordà, Northern Spain). *J. Hydrol.* **2011**, *409*, 407–422. [CrossRef]
46. Akay, E.; Uysal, Ş.; Poisson, A.; Cravatte, J.; Muller, C. Stratigraphy of the Antalya Neogene Basin. *Bull. Geol. Soc. Turk.* **1985**, *28*, 105–119.
47. Poisson, A.; Wernli, R.; Sağular, E.K.; Temiiz, H. New Data Concerning the Age of the Aksu Thrust in the South of the Aksu Valley, Isparta Angle (SW Turkey): Consequences for the Antalya Basin and the Eastern Mediterranean. *Geol. J.* **2003**, *38*, 311–327. [CrossRef]
48. Pentecost, A. The Quaternary Travertine Deposits of Europe and Asia Minor. *Quat. Sci. Rev.* **1995**, *14*, 1005–1028. [CrossRef]
49. Pentecost, A.; Lord, T. Postglacial Tufas and Travertines from the Craven District of Yorkshire. *Cave Sci.* **1988**, *15*, 15–19.
50. Ordóñez, S.; García del Cura, M.A. Recent and Tertiary Fluvial Carbonates in Central Spain. In *Modern and Ancient Fluvial Systems*; Collinson, J.D., Lewin, J., Eds.; Blackwell Scientific Publications: Cambridge, UK, 1983; pp. 485–497.
51. Chafetz, H.S.; Folk, R.L. Travertines; Depositional Morphology and the Bacterially Constructed Constituents. *J. Sediment. Res.* **1984**, *54*, 289–316. [CrossRef]
52. Pedley, H.M. Classification and Environmental Models of Cool Freshwater Tufas. *Sediment. Geol.* **1990**, *68*, 143–154. [CrossRef]

53. Uçar, F. Determination of Karstic Activity by Utilizing 2-Dimensional Electrical Resistivity Method. Master's Thesis, Akdeniz University, Antalya, Türkiye, 2014.
54. Putiska, R.; Kusnirak, D.; Dostal, I.; Lacny, A.; Mojzes, A.; Hok, J.; Pasteka, R.; Krajnak, M.; Bosansky, M. Integrated Geophysical and Geological Investiga-tions of Karst Structures in Komberek, Slovakia. *J. Cave Karst Stud.* **2014**, *76*, 155–163. [CrossRef]
55. Haldar, S.K. Exploration Geophysics. In *Mineral Exploration Principles and Applications*, 2nd ed.; Elsevier: Amsterdam, The Netherlands, 2018; pp. 103–122.
56. Olayinka, A.I.; Yaramanci, U. Assessment of the Reliability of 2D Inversion of Apparent Resistivity Data. *Geophys. Prospect.* **2000**, *48*, 293–316. [CrossRef]
57. Madden, T.R. The Resolving Power of Geoelectric Measurements for Delineating Resistive Zones within the Crust. In *The Structure and Physical Properties of the Earth's Crust*; Heacock, J.G., Ed.; Geophysical Monograph Series; American Geophysical Union: Washington, DC, USA, 1971; Volume 14, pp. 95–105.
58. Mufti, I.R. Finite-Difference Resistivity Modeling for Arbitrarily Shaped Two-Dimensional Structures. *Geophysics* **1976**, *41*, 62–78. [CrossRef]
59. Dey, A.; Morrison, H.F. Resistivity Modelling for Arbitrarily Shaped Three-Dimensional Structures. *Geophysics* **1979**, *44*, 753–780. [CrossRef]
60. Tong, L.-T.; Yang, C.-H. Incorporation of Topography into Two-Dimensional Resistivity Inversion. *Geophysics* **1990**, *55*, 354–361. [CrossRef]
61. Eskola, L.; Soininen, H.; Oksama, M. Modeling of Resistivity and IP Anomalies of a Thin Conductor with an Integral Equation. *Geoexploration* **1989**, *26*, 95–104. [CrossRef]
62. Telford, W.M.; Geldart, L.P.; Sheriff, R.E. *Applied Geophysics*, 2nd ed.; Cambridge University Press: Cambridge, UK, 1990; p. 792.
63. Dahlin, T. *RES2DINV, 2D Resistivity and IP Inversion Software, 3.5*; Geotomo Software, LLC: Houston, TX, USA, 2004.
64. Loke, M.H.; Dahlin, T. A Comparison of the Gauss-Newton and Quasi-Newton Methods in Resistivity Imaging Inversion. *J. Appl. Geophys.* **2002**, *49*, 149–162. [CrossRef]
65. Loke, M.H.; Barker, R.D. Rapid Least-Squares Inversion of Apparent Resistivity Pseudosections by a Quasi-Newton Method. *Geophys. Prospect.* **1996**, *44*, 131–152. [CrossRef]
66. *IPI2WIN, Resistivity Sounding Interpretation Software*, 3.0.1; Geoscan-M Ltd.: Moscow, Russia, 2003.
67. *Surfer 10.2.601*; Golden Software, LLC: Golden, CO, USA, 2011.
68. Nouioua, I.; Rouabhia, A.; Fehdi, C.; Boukelloul, M.L.; Gadri, L.; Chabou, D.; Mouici, R. The Application of GPR and Electrical Resistivity Tomography as Useful Tools in Detection of Sinkholes in the Cheria Basin (Northeast of Algeria). *Environ. Earth Sci.* **2012**, *68*, 1661–1672. [CrossRef]
69. Bobachev, A.; Modin, I.; Shevinin, V. *IPI2Win V2.0: User's Guide*; Geoscan-M Ltd.: Moscow, Russia, 2003; p. 15.

Disclaimer/Publisher's Note: The statements, opinions and data contained in all publications are solely those of the individual author(s) and contributor(s) and not of MDPI and/or the editor(s). MDPI and/or the editor(s) disclaim responsibility for any injury to people or property resulting from any ideas, methods, instructions or products referred to in the content.